



## Research Article

# Lineshape of Magnetic Resonance and Its Effects on Free Induction Decay and Steady-State Free Precession Signal Formation

C. H. Ziener <sup>1,2</sup>, M. Uhrig,<sup>1</sup> T. Kampf,<sup>3,4</sup> V. J. F. Sturm,<sup>2</sup> F. T. Kurz,<sup>1,2</sup> S. Heiland,<sup>2</sup> M. Bendszus,<sup>2</sup> M. Pham,<sup>4</sup> P. M. Jakob,<sup>3</sup> H.-P. Schlemmer,<sup>1</sup> and L. R. Buschle <sup>1</sup>

<sup>1</sup>German Cancer Research Center (DKFZ), Department of Radiology (E010), Im Neuenheimer Feld 280, 69120 Heidelberg, Germany

<sup>2</sup>Heidelberg University Hospital, Department of Neuroradiology, Im Neuenheimer Feld 400, 69120 Heidelberg, Germany

<sup>3</sup>University of Würzburg, Department of Experimental Physics 5, Am Hubland, 97074 Würzburg, Germany

<sup>4</sup>Würzburg University Hospital, Department of Diagnostic and Interventional Neuroradiology, Josef-Schneider-Straße 11, 97080 Würzburg, Germany

Correspondence should be addressed to L. R. Buschle; [l.buschle@dkfz.de](mailto:l.buschle@dkfz.de)

C. H. Ziener and M. Uhrig contributed equally to this work.

Received 31 March 2019; Revised 28 June 2019; Accepted 13 August 2019; Published 19 January 2020

Academic Editor: Giacomo Parigi

Copyright © 2020 C. H. Ziener et al. This is an open access article distributed under the Creative Commons Attribution License, which permits unrestricted use, distribution, and reproduction in any medium, provided the original work is properly cited.

Magnetic resonance imaging based on steady-state free precision (SSFP) sequences is a fast method to acquire  $T_1$ ,  $T_2$ , and  $T_2^*$ -weighted images. In inhomogeneous tissues such as lung tissue or blood vessel networks, however, microscopic field inhomogeneities cause a nonexponential free induction decay and a non-Lorentzian lineshape. In this work, the SSFP signal is analyzed for different prominent tissue models. Neglecting the effect of non-Lorentzian lineshapes can easily result in large errors of the determined relaxation times. Moreover, sequence parameters of SSFP measurements can be optimized for the nonexponential signal decay in many tissue structures.

## 1. Introduction

Magnetic resonance imaging is a powerful tool for *in vivo* measurements with different tissue contrasts. Most common tissue contrasts are based on  $T_1$ -,  $T_2$ -, or  $T_2^*$ -weighted images, but also susceptibility-weighted, diffusion-weighted, or contrast-enhanced imaging are used in clinical standard routine. Recently, much effort has been put into a quantitative measurement of the underlying tissue parameters. This would allow an improved diagnosis with measurements performed on different dates and scanners. Moreover, most big data analyses rely on quantitative reliable contrast parameters. Typically, the measurement times of quantitative  $T_1$  and  $T_2$  maps are long. Recently, a promising method called MR fingerprinting was developed for quantitative determination of  $T_1$  and  $T_2$  with short measurement times. The basic idea of MR fingerprinting is to apply pulses, echo times, and acquisition times (pseudo) randomly and to compare the measurements with previously calculated dictionaries [1]. A typical implementation of a MR

fingerprinting approach is performed with a steady-state free precession (SSFP) sequence.

Moreover, quantitative blood oxygenation level dependent (qBOLD) measurements in functional magnetic resonance imaging (fMRI) might be a relevant application for SSFP sequences. So far, qBOLD measurements are based on FLASH-like MR sequences and evaluated with analytical solutions of the Bloch- or the Bloch-Torrey-equation [2–5]. However, a quantitative evaluation of the SSFP sequence for blood vessel networks might lead to the applicability of SSFP for qBOLD measurements [6], similar than used for detection of microstructural properties in the heart [7].

For nonhomogeneous tissues, susceptibility differences between different compartments cause magnetic field inhomogeneities, and the gradient echo and spin echo signal decay cannot be described sufficiently by monoexponential decays. Typical examples are vessel networks in the brain [8–11], around axons [12], or in the myocardium, causing magnetic field inhomogeneities due to the susceptibility

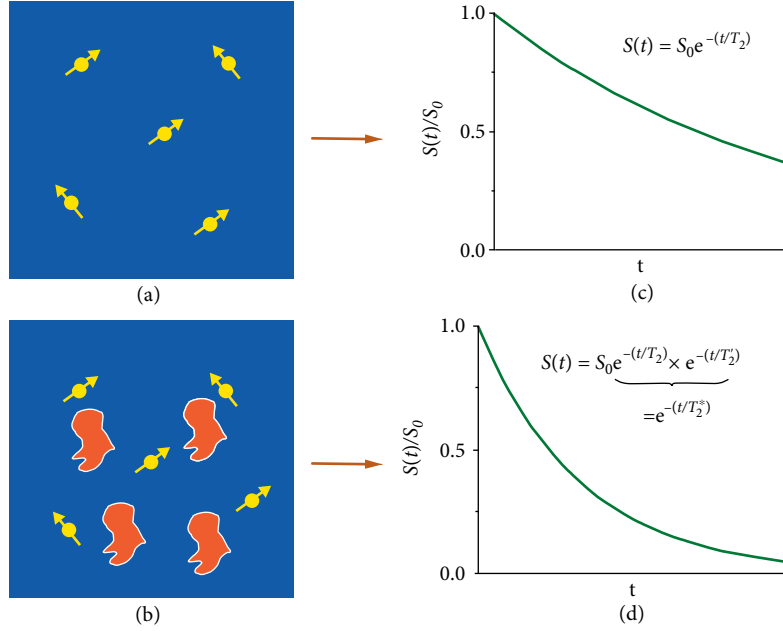


FIGURE 1: Free induction decay for dephasing in the absence and presence of microscopic magnetic field inhomogeneities. In the case of homogeneous tissue (a), the intrinsic transverse relaxation leads to purely monoexponential signal decay with the intrinsic transverse relaxation time  $T_2$  as shown in (c). In the presence of microscopic magnetic field inhomogeneities (b), dephasing effects cause an additional decay of the signal that might be approximated by a monoexponential relaxation time  $T_2'$ . (d) The intrinsic relaxation times  $T_2$  and  $T_2'$  are combined to the relaxation times  $T_2^*$ .

difference between blood and tissue [13–15]. Although imaging of lung tissue is typically performed with computed tomography, in recent years, enormous efforts have been put into the field of lung MRI [16–19]. Transverse relaxation in lung tissue is dominated by susceptibility effects between spherically shaped alveoli and surrounding tissues that cause nonexponential signal decay [20–22]. Similarly, cells labeled with magnetic particles produce magnetic field inhomogeneities leading to an accelerated dephasing [23, 24]. So far, the SSFP signal was typically analyzed under the assumption of exponential signal decay. In this work, the free induction decay and the SSFP signal is analyzed for different types of tissue structures where the signal decay is nonexponential. The results are relevant for a detailed understanding of the SSFP signal, for example for quantitative MRI including MR fingerprinting.

As visualized in Figure 1(a), an ensemble of spin-bearing particles in an external magnetic field along the  $z$ -axis leads to a macroscopic magnetization. Due to spin-spin-interaction, the transverse signal  $S(t)$  decays purely monoexponentially (see Figure 1(c)) with the intrinsic relaxation time  $T_2$ . In the presence of magnetic field inhomogeneities (see Figure 1(b)), an additional modulation  $M(t)$  of the signal results from dephasing inside the local magnetic field:

$$\frac{S(t)}{S(0)} = e^{-t/T_2} \frac{M(t)}{M(0)}. \quad (1)$$

For negligible diffusion effects, this modulation depends on the response function  $M_x(\omega) + iM_y(\omega)$  of the applied pulse sequence as well as on the distribution of the local Larmor frequencies  $p(\omega)$ , which is also denoted as lineshape:

$$M(t) = \int_{-\infty}^{+\infty} d\omega p(\omega) [M_x(\omega) + iM_y(\omega)] e^{-i\omega t}. \quad (2)$$

In general, the lineshape  $p(\omega)$  depends on the geometry of the underlying structures creating microscopic field inhomogeneities, and the magnetization is nonexponential [25, 26]. Even though, usually a Lorentzian lineshape (index “L”) in the form of

$$p_L(\omega) = \frac{T_2'}{\pi} \frac{1}{1 + [\omega T_2']^2} \quad (3)$$

is assumed to describe the resulting Larmor frequency distribution of the underlying tissue [27]. In the case of a FLASH-sequence with repetition time  $T_R$  and flip angle  $\alpha$ , the response function takes the frequency-independent and purely real form [28]:

$$M_x(\omega) + iM_y(\omega) = M_0 \sin(\alpha) \frac{1 - e^{-(T_R/T_1)}}{1 - e^{-(T_R/T_1)} \cos(\alpha)}. \quad (4)$$

By virtue of Equation (3), the corresponding magnetization (also denoted with index “L”) decays monoexponentially:

$$\frac{M_L(t)}{M_L(0)} = e^{-t/T_2^*}, \quad (5)$$

which results in a purely monoexponential signal decay  $S(t)$  with relaxation time  $T_2^*$  as shown in Figure 1(d). The goal of this work is to overcome the monoexponential approximation of the magnetization by utilizing the lineshapes of specific tissue geometries.

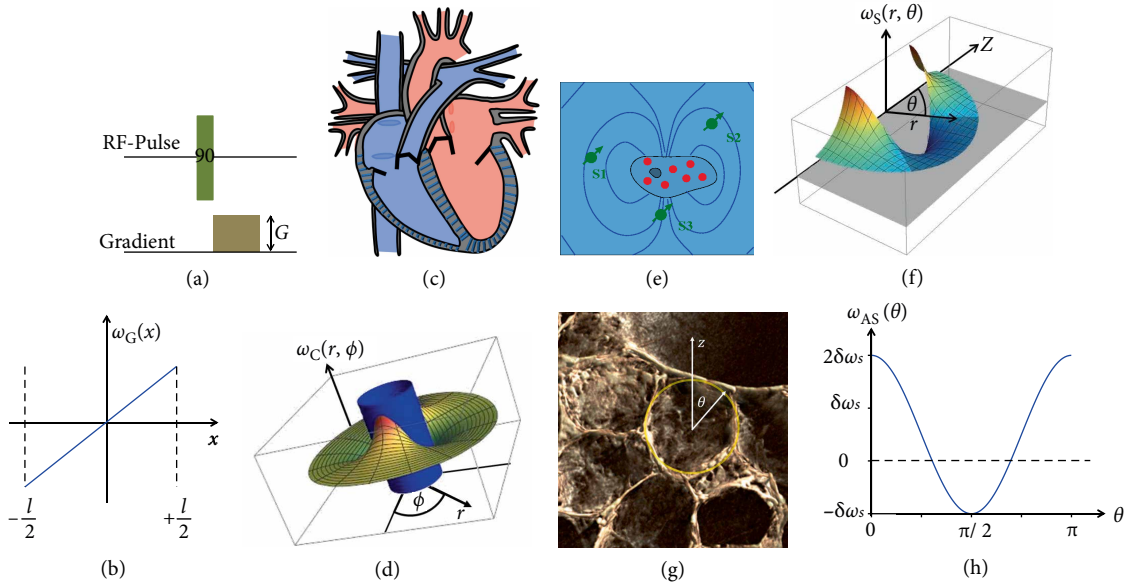


FIGURE 2: Larmor-frequencies for different local magnetic field inhomogeneities. For dephasing in an imaging gradient or diffusion weighted gradient (a) the local resonance frequency is proportional to the spatial coordinate (b) according to Equation (6). In case of cylindrical objects, as for example blood filled capillaries in the myocardium (c) the local Larmor frequency exhibits the form of a two-dimensional dipole field (d) according to Equation (7) where  $r$  and  $\phi$  are polar coordinates in a plane perpendicular to the axis of the vessel. Dephasing around spherical objects as exemplified by magnetically labeled cells (e) is described by the three-dimensional dipole field with low volume fraction  $\eta = V_{\text{sir}}/V_{\text{total}} \ll 1$  or its extended version (f) according to Equation (8) or Equation (10). On the alveolar surface ( $\eta = 1$ ) (g) [image adapted from [18]], the resonance frequency depends on the polar angle  $\theta$  only (h).

## 2. Material and Methods

In this work, the SSFP signal of important tissue geometries is derived. Therefore, the underlying local Larmor frequencies as well as the resulting lineshapes for the important cases of dephasing in a constant gradient as well as dephasing in a two-dimensional and three-dimensional dipole field (see Figure 2) are reviewed (see Sections 2.1 and 2.2). Then, the mathematical description of SSFP signal formation is introduced (Section 2.3), while new results are presented in Section 3.

**2.1. Local Larmor Frequencies.** Externally applied magnetic field gradients or internal gradients due to susceptibility differences cause a local magnetic field which is associated with a local Larmor frequency in which the dephasing occurs. The most important case is the dephasing in a constant gradient  $G = \Delta B/l$ . Without loss of generality, the gradient is applied in  $x$ -direction (see Figure 2(a)) within the interval  $-l/2 \leq x \leq +l/2$  (see Figure 2(b)). The Larmor frequency  $\omega_G(x) = \gamma Gx$  takes the form of

$$\omega_G(x) = \delta\omega_G \frac{x}{l}, \quad (6)$$

where  $\delta\omega_G = \gamma \Delta B = \gamma G l$  is denoted as the characteristic frequency.

Cylindrical objects as for example blood filled vessels in the myocardium or in skeletal muscle (see Figure 2(c)) induce a two-dimensional dipole field [29]. The corresponding local Larmor frequency around these vessels is given by

$$\omega_C(r, \phi) = \delta\omega_C R_C^2 \frac{\cos(2\phi)}{r^2}, \quad (7)$$

where  $r$  and  $\phi$  are polar coordinates in a plane perpendicular to the axis of the cylindrical object (see Figure 2(d)), and  $R_C$  denotes the radius of the vessels. The strength of the dipole field depends on the susceptibility differences  $\Delta\chi_C$  between blood inside the vessel and surrounding tissue, as well as the angle  $\vartheta$  between vessel and main magnetic field:  $\delta\omega_C = \gamma B_0 \sin^2(\vartheta) \Delta\chi_C / 2$ .

Spherical magnetic field inhomogeneities, such as magnetically labeled cells or alveoli of the lung (see Figure 2(e) and [30]), create a three-dimensional dipole field

$$\omega_S(r, \theta) = \delta\omega_S R_S^3 \frac{3\cos^2(\theta) - 1}{r^3}, \quad (8)$$

which depends on the distance  $r$  to the center of the sphere and the polar angle  $\theta$  between the external magnetic field and the position vector as visualized in Figure 2(f). In the lung, the dipole field strength depends on the susceptibility difference  $\Delta\chi_S$  between air-filled alveoli and surrounding tissue:  $\delta\omega_S = \gamma B_0 \Delta\chi_S / 3$ .

If the dephasing is restricted to the surface of a spherical object with radius  $R_S$ , as for example on the surface of an alveolus as visualized in Figure 2(g), the radius  $r$  in Equation (8) always takes the value  $r = R_S$ . Thus, the local Larmor frequency on the alveolar surface (index AS) depends on the polar angle  $\theta$  only:

$$\omega_{AS}(\theta) = \delta\omega_S [3\cos^2(\theta) - 1]. \quad (9)$$

As visualized in Figure 2(h), the maximal frequency takes the value  $+2\delta\omega_s$  for  $\theta = 0$  and  $\theta = \pi$ , while the minimal frequency takes the value  $-\delta\omega_s$  for  $\theta = \pi/2$ . While the alveolar surface model is valid for air volume fractions close to  $\eta = V_{\text{air}}/V_{\text{total}} \rightarrow 1$ , recently, the alveolar surface model was extended to air volume fractions  $\eta \geq 0.5$  [31]. In this extended alveolar surface model (index EAS), the Larmor frequency around an alveolus was approximated by:

$$\omega_{\text{EAS}}(r, \theta) = \delta\omega_s R_S^2 \frac{3 \cos^2(\theta) - 1}{r^2}. \quad (10)$$

If the movement of the spin-bearing particles is restricted to the alveolar surface, the extended alveolar surface model agrees with the alveolar surface model. However, it yields more realistic results for particles being not exactly restricted but diffusing close to the alveolar surface [31].

**2.2. Corresponding Lineshapes.** As in detail shown in Appendix A, the magnetic field inhomogeneities described by the local Larmor frequency offsets  $\omega(\mathbf{r})$  lead to dephasing of the local magnetization and a decay of the total magnetization  $M(t)$ . However, it is more convenient to analyze the frequency distribution or lineshape  $p(\omega)$  that is connected via a Fourier transform with the magnetization  $M(t)$ . The lineshapes

$$p_C(\omega) = \begin{cases} \frac{\eta}{1-\eta} \frac{\delta\omega_c}{\pi\omega^2} \sqrt{1 - \left[\frac{\omega}{\delta\omega_c}\right]^2} & \text{for } \frac{\omega}{\delta\omega_c} \leq -\eta \text{ or } \frac{\omega}{\delta\omega_c} \geq \eta, \\ \frac{\eta}{1-\eta} \frac{\delta\omega_c}{\pi\omega^2} \left[ \sqrt{1 - \left[\frac{\omega}{\delta\omega_c}\right]^2} - \sqrt{1 - \left[\frac{\omega}{\eta\delta\omega_c}\right]^2} \right] & \text{for } -\eta \leq \frac{\omega}{\delta\omega_c} \leq \eta, \\ 0 & \text{otherwise.} \end{cases} \quad (12)$$

Details of the derivation can be found in [34]. This lineshape is visualized in Figure 3(b). The lineshape of a single vessel in a cubic voxel is numerically and analytically determined in [35–37], the lineshape of randomly distributed vessels being analyzed in [8]. A detailed comparison between randomly distributed vessels and the single vessel model is given in Appendix A in [11].

$$p_S(\omega) = \begin{cases} \frac{\eta}{3\sqrt{3}[1-\eta]} \frac{\delta\omega_s}{\omega^2} \left[ 2 - \frac{\omega}{\delta\omega_s} \right] \sqrt{1 + \frac{\omega}{\delta\omega_s}} & \text{for } \frac{\omega}{\delta\omega_s} \leq -\eta \text{ or } \frac{\omega}{\delta\omega_s} \geq 2\eta, \\ \frac{\eta}{3\sqrt{3}[1-\eta]} \frac{\delta\omega_s}{\omega^2} \left[ \left[ 2 - \frac{\omega}{\delta\omega_s} \right] \sqrt{1 + \frac{\omega}{\delta\omega_s}} - \left[ 2 - \frac{\omega}{\eta\delta\omega_s} \right] \sqrt{1 + \frac{\omega}{\eta\delta\omega_s}} \right] & \text{for } -\eta \leq \frac{\omega}{\delta\omega_s} \leq 2\eta, \\ 0 & \text{otherwise.} \end{cases} \quad (13)$$

Details of the derivation can be found in [38]. This lineshape is visualized in Figure 3(d). Numerical simulations of a single alveolus in spherical and cubic voxels were performed in [39, 40]. Randomly distributed spheres are considered in [8].

In the limit of restricting water molecules to the surface of the alveoli, the lineshape is given by (see also the corresponding local Larmor frequency given in Equation (9)):

$$p_{\text{AS}}(\omega) = \lim_{\eta \rightarrow 1} p_S(\omega) = \begin{cases} \frac{1}{2\delta\omega_s \sqrt{3}[(\omega/\delta\omega_s)+1]} & \text{for } -1 \leq \frac{\omega}{\delta\omega_s} \leq +2, \\ 0 & \text{elsewhere.} \end{cases} \quad (14)$$

This expression also follows from the lineshape caused by a spherical object given in Equation (13) in the limit  $\eta \rightarrow 1$  when dephasing occurs on the surface of the sphere:  $p_{\text{AS}}(\omega) = \lim_{\eta \rightarrow 1} p_S(\omega)$ .

corresponding to the above described frequency offsets are reviewed in this subsection. The relevant expressions for the magnetization decay  $M(t)$  can be found in Appendix B.

A monoexponential magnetization decay with relaxation time  $T_2'$  results in a Lorentzian lineshape as given in Equation (3) and shown in Figure 3(a). Note that the intrinsic  $T_2$  relaxation time is absorbed in the definition of the magnetization  $M(t)$ , see Equation (1).

For dephasing in the constant gradient  $\omega_G(x)$  given in Equation (6), the lineshape is a boxcar function

$$p_G(\omega) = \begin{cases} \frac{1}{\delta\omega_G} & \text{for } -\frac{1}{2} \leq \frac{\omega}{\delta\omega_G} \leq +\frac{1}{2}, \\ 0 & \text{elsewhere,} \end{cases} \quad (11)$$

and all possible Larmor frequencies take the same probability  $1/\delta\omega_G$ . Since the interval  $-1/2 \leq x \leq +1/2$  is considered, frequencies exclusively occur within the range  $-\delta\omega_G/2 \leq \omega \leq +\delta\omega_G/2$ . The lineshape is visualized in Figure 3(c). Dephasing and diffusion in constant gradients have intensively been analyzed *e.g.*, in [32, 33].

The lineshape caused by a two-dimensional dipole field around a cylindrical object (see Figure 2(d)) depends on the volume fraction  $\eta = R_C^2/R_D^2$ , where  $R_D$  constitutes the radius of the surrounding dephasing cylinder:

The asymmetric lineshape caused by the three-dimensional dipole field (see Equation (8)) around a spherical object (see Figure 2(f)) also depends on the volume fraction  $\eta = R_S^3/R_D^3$ , where  $R_D$  represents the radius of the surrounding dephasing sphere:

In the extended alveolar surface model, the lineshape was obtained as [31]:

$$p_{\text{EAS}}(\omega) = \begin{cases} \frac{\eta}{1-\eta} \frac{3\sqrt{3}}{16} \frac{\delta\omega_s}{\omega^2} \left[ \left[ 1 - \frac{2}{3} \frac{\omega}{\delta\omega_s} \right] \sqrt{1 + \frac{\omega}{\delta\omega_s}} + f\left(\frac{\omega}{\delta\omega_s}\right) \right] & \text{for } -1 \leq \frac{\omega}{\delta\omega_s} \leq +2, \\ 0 & \text{elsewhere,} \end{cases} \quad (15)$$

where the function  $f(\omega/\delta\omega_s)$  is defined in Equation (D.1) in Appendix D. The lineshape  $p_{\text{EAS}}(\omega)$  also converges to the alveolar surface lineshape (see Equation (14)) in the limit:  $\lim_{\eta \rightarrow 1} p_{\text{EAS}}(\omega) = p_{\text{AS}}(\omega)$ .

**2.3. SSFP Signal Formation.** A pulse sequence similar to the previously described FLASH-sequence is the balanced SSFP-sequence [41]. While the FLASH-sequence spoils residual transverse magnetization before the following excitation pulse, the SSFP-sequence reverses the effects of the applied gradients.

After preparation in the steady state of a SSFP sequence, two different phase cycles for the excitation pulse are common: alternating phase and constant phase. The response function of the SSFP-sequence for alternating phase (upper sign) and constant phase (lower sign) is given as (see Equation (1) in [42]):

$$M_x^\pm(\omega) + iM_y^\pm(\omega) = M_0[1 - E_1] \sin(\alpha) \frac{1 \mp E_2 e^{+i\omega T_R}}{p \mp q \cos(\omega T_R)}, \quad (16)$$

with the parameters

$$p = 1 - E_1 E_2^2 + [E_2^2 - E_1] \cos(\alpha), \quad (17)$$

$$q = E_2 [1 - E_1] [1 + \cos(\alpha)], \quad (18)$$

and the abbreviations

$$E_1 = e^{-(T_R/T_1)} \text{ and } E_2 = e^{-(T_R/T_2)}. \quad (19)$$

For further analysis it is advantageous, to expand the response function in a Fourier series [43, 44]

$$M_x^\pm(\omega) + iM_y^\pm(\omega) = M_0 \sum_{k=-\infty}^{+\infty} F_k^\pm e^{-ik\omega T_R}, \quad (20)$$

where the Fourier coefficients are given as

$$F_k^\pm = \frac{1 - E_1}{\sqrt{p^2 - q^2}} \sin(\alpha) [1 + E_2 z^{\Theta(k)}] [\mp z]^{|k|}, \quad (21)$$

with the series expansion point

$$z = \sqrt{\frac{p^2}{q^2} - 1} - \frac{p}{q}, \quad (22)$$

and the step function of the discrete variable  $k$ :

$$\Theta(k) = \begin{cases} +1 & \text{for } k \geq 0, \\ -1 & \text{for } k < 0. \end{cases} \quad (23)$$

In Figure 4, the Fourier coefficients are visualized for different flip angles  $\alpha$ . This agrees with numerical results for the coefficients obtained by Kim and Cho [45].

Finally, the total signal that is measured depends on the intrinsic  $T_2$ -relaxation time, the lineshape  $p(\omega)$ , and the response function of the underlying pulse sequence  $M_x^\pm(\omega) + iM_y^\pm(\omega)$  (see Equation (5) in [46]):

$$S^\pm(t) = e^{-(t/T_2)} \int_{-\infty}^{+\infty} d\omega p(\omega) [M_x^\pm(\omega) + iM_y^\pm(\omega)] e^{-i\omega t}. \quad (24)$$

Thus, for detailed understanding of SSFP signal formation, it is mandatory to consider the exact lineshape as presented in the last subsection.

### 3. Results

Introducing the Fourier series of the response function (20) in the general expression for the signal (24) and considering

the analytic continuation of the free induction decay for negative times in Equation (A.7), the SSFP signal  $S^\pm(t)$  can be expressed in terms of the Fourier coefficients  $F_k^\pm$  and the free induction decay  $M(t)$

$$S^\pm(t) = e^{-(t/T_2)} M_0 \quad (25)$$

$$\times \left[ F_0^\pm \frac{M(t)}{M(0)} + \sum_{k=1}^{\infty} \left[ F_{+k}^\pm \frac{M(kT_R + t)}{M(0)} + F_{-k}^\pm \frac{M^*(kT_R - t)}{M(0)} \right] \right].$$

In the following subsections, this general expression is evaluated for the specific field inhomogeneities as described in section "Material and methods".

**3.1. Lorentzian Lineshape.** To obtain the SSFP signal for the Lorentzian lineshape given in (3), it is advantageous to introduce the corresponding purely monoexponential magnetization decay from Equation (5) into the general expression (25). The appearing sums over the Fourier coefficients can be traced back to geometric series, and finally the signal is a sum of an exponentially decaying part  $\propto \exp(-t[1/T_2 + 1/T_2']) = \exp(-t/T_2')$  and an exponentially growing part  $\propto \exp(-t[1/T_2 - 1/T_2'])$

$$\frac{S_{L,0}^\pm(t)}{S_{L,0}^\pm} = e^{-(t/T_2)} \left[ \gamma^\pm e^{+(t/T_2')} + [1 - \gamma^\pm] e^{-(t/T_2')} \right] \quad (26)$$

with the prefactor  $\gamma^\pm$  and the abbreviation  $E_2'$

$$\frac{1}{\gamma^\pm} = 1 \mp \frac{1 + zE_2}{[z + E_2]E_2'}, \quad (27)$$

$$E_2' = e^{-(T_R/T_2')}, \quad (28)$$

as well as the initial signal  $S_{L,0}^\pm = S_{L,0}^\pm(0)$

$$S_{L,0}^\pm = M_0 \frac{1 - E_1}{\sqrt{p^2 - q^2}} \sin(\alpha) \frac{1 + zE_2 \mp [z + E_2]E_2'}{1 \pm zE_2'}. \quad (29)$$

Measuring the SSFP signal allows fitting the relaxation times  $T_2, T_2'$ , and the prefactor  $\gamma^\pm$ . The next subsection describes how to obtain the relaxation time  $T_1$  knowing these parameters.

**3.2. Quantification of the Longitudinal Relaxation Time.** The series expansion point  $z$  can be obtained after several rearrangement steps from the prefactor  $\gamma^\pm$  given in Equation (27):

$$z = \frac{E_2 E_2' [\gamma^+ - 1] - \gamma^+}{E_2' [1 - \gamma^+] + E_2 \gamma^+} = \frac{E_2 E_2' [\gamma^- - 1] + \gamma^-}{E_2' [1 - \gamma^-] - E_2 \gamma^-} \quad (30)$$

$$= \frac{E_2 E_2' [\gamma^\pm - 1] \mp \gamma^\pm}{E_2' [1 - \gamma^\pm] \pm E_2 \gamma^\pm}.$$

The definition of the series expansion point in Equation (22) leads to the relation  $1 + z^2 = -2zp/q$ . Introducing the explicit expressions for the parameters  $p$  and  $q$  according to Equations (17) and (18), after several rearrangement steps one obtains:

$$E_1 = \frac{E_2[z^2 + 1][\cos(\alpha) + 1] + 2z[E_2^2 \cos(\alpha) + 1]}{E_2[z^2 + 1][\cos(\alpha) + 1] + 2z[\cos(\alpha) + E_2^2]}. \quad (31)$$

In case of a Lorentzian lineshape, the parameters  $\gamma^\pm$ ,  $E_2$ , and  $E_2'$  can be determined by a biexponential model fit (see Equation (26)). Thus, the series expansion point  $z$  can be calculated according to Equation (30), and the relaxation time is yielded by utilizing Equation (31).

**3.3. Constant Gradient.** In the case of constant gradients, the time evolution of the magnetization according to Equation (B.1) has to be introduced into the general expression for the SSFP signal in Equation (25):

$$\begin{aligned} S_G^\pm(t) = & e^{-(t/T_2)} M_0 \frac{1 - E_1}{\sqrt{p^2 - q^2}} \sin(\alpha) \frac{2}{\delta\omega_G} \frac{1 + zE_2}{t} \\ & \cdot \operatorname{Im} \left( {}_2F_1 \left( 1, \frac{t}{T_R}; 1 + \frac{t}{T_R}; \mp z e^{i\delta\omega_G(T_R/2)} \right) e^{i\delta\omega_G(t/2)} \right) \\ & \mp e^{-(t/T_2)} M_0 \frac{1 - E_1}{\sqrt{p^2 - q^2}} \sin(\alpha) \frac{2}{\delta\omega_G} \frac{z + E_2}{T_R - t} \\ & \cdot \operatorname{Im} \left( {}_2F_1 \left( 1, 1 - \frac{t}{T_R}; 2 - \frac{t}{T_R}; \mp z e^{i\delta\omega_G(T_R/2)} \right) e^{i\delta\omega_G(T_R - t/2)} \right), \end{aligned} \quad (32)$$

where  ${}_2F_1$  denotes the Gaussian or ordinary hypergeometric function. At the initial time  $t = 0$ , the signal becomes:

$$\begin{aligned} \frac{S_G^\pm(0)}{M_0} = & \frac{1 - E_1}{\sqrt{p^2 - q^2}} \sin(\alpha) \\ & \cdot \left[ 1 + E_2 z \mp \frac{4 + 2E_2[z + (1/z)]}{\delta\omega_G T_R} \arctan \left( \frac{z \sin(\delta\omega_G T_R/2)}{1 \pm z \cos(\delta\omega_G T_R/2)} \right) \right]. \end{aligned} \quad (33)$$

Since the lineshape for dephasing in a constant gradient is a symmetric function (see Equation (11) and Figure 3(b)), the SSFP signal for dephasing in a constant gradient is purely real.

**3.4. Alveolar Surface.** To find the SSFP signal for dephasing on the alveolar surface, the relevant magnetization given in Equation (B.6) has to be introduced in the general expression for the SSFP signal in Equation (25). Finally, the SSFP signal for dephasing on the alveolar surface is given by

$$\begin{aligned} S_{AS}^\pm(t) = & e^{-(t/T_2)} M_0 \frac{1 - E_1}{\sqrt{p^2 - q^2}} \sin(\alpha) \frac{1 + i}{2} \sqrt{\frac{\pi}{6}} e^{i\delta\omega_s t} \\ & \cdot \left[ \frac{1 + E_2 z}{\sqrt{\delta\omega_s t}} \operatorname{erfi} \left( [1 - i] \sqrt{3\delta\omega_s \frac{t}{2}} \right) \right. \\ & + [1 + E_2 z] \sum_{k=1}^{\infty} \frac{e^{+i\delta\omega_s k T_R} [\mp z]^k}{\sqrt{\delta\omega_s [k T_R + t]}} \operatorname{erfi} \left( [1 - i] \sqrt{3\delta\omega_s \frac{k T_R + t}{2}} \right) \\ & \left. + [1 + E_2 z^{-1}] \sum_{k=1}^{\infty} \frac{e^{-i\delta\omega_s k T_R} [\mp z]^k}{\sqrt{\delta\omega_s [k T_R - t]}} \operatorname{erfi} \left( [1 - i] \sqrt{3\delta\omega_s \frac{k T_R - t}{2}} \right) \right]. \end{aligned} \quad (34)$$

The initial signal follows as

$$\begin{aligned} \frac{S_{AS}^\pm(0)}{M_0} = & \frac{1 - E_1}{\sqrt{p^2 - q^2}} \sin(\alpha) [1 + E_2 z] + \frac{1 - E_1}{\sqrt{p^2 - q^2}} \sin(\alpha) \frac{1 + i}{2} \sqrt{\frac{\pi}{6}} \\ & \cdot \left[ [1 + E_2 z] \sum_{k=1}^{\infty} \frac{e^{+i\delta\omega_s k T_R}}{\sqrt{\delta\omega_s k T_R}} [\mp z]^k \operatorname{erfi} \left( [1 - i] \sqrt{3\delta\omega_s \frac{k T_R}{2}} \right) \right. \\ & \left. + [1 + E_2 z^{-1}] \sum_{k=1}^{\infty} \frac{e^{-i\delta\omega_s k T_R}}{\sqrt{\delta\omega_s k T_R}} [\mp z]^k \operatorname{erfi} \left( [1 - i] \sqrt{3\delta\omega_s \frac{k T_R}{2}} \right) \right]. \end{aligned} \quad (35)$$

Similar expressions can also be derived for the extended alveolar surface model.

So far, the SSFP signal was usually described under the assumption of Lorentzian lineshapes. A comparison of both lineshapes is shown in Figure 5, together with the response functions  $M_x(\omega)$  and  $M_y(\omega)$ . In Figure 6, the initial signal  $S_{L,0}^\pm$  that determines the signal to noise ratio is compared in the Lorentzian lineshape model and the alveolar surface model in dependence on the sequence parameters  $T_R$  and  $\alpha$ . Even both curves share the general characteristic form, there exist obvious differences between the Lorentzian lineshape and the alveolar surface model: the signal in the alveolar surface model is complex-valued and shows oscillation whereas the Lorentzian lineshape model exhibits only a purely real  $x$ -component of the signal.

**3.5. Numerical Validation.** To validate the theoretical findings, numerical simulations were performed. A steady-state signal can be measured in the equilibrium state after applying a certain number of rf pulses. The signal after the  $(n + 1)$ -th rf-pulse depends on the pulse structure, the relaxation times and the precession frequency. It can be written as:

$$\mathbf{S}_{n+1} = \mathbf{P} \cdot [\mathbf{R}(\omega, T_R) \cdot \mathbf{S}_n + \mathbf{\Lambda}(T_R)] \quad (36)$$

where the matrix  $\mathbf{P}$  describes the influence of the rf pulses, the matrix  $\mathbf{R}$  gives the relaxation of the signal as well as the phase precession according to the Larmor frequency, and  $\mathbf{\Lambda}$  denotes a vector driving the magnetization to thermal equilibrium. The matrices are given as [47]:

$$\mathbf{P} = \begin{pmatrix} \cos(\alpha) & 0 & \sin(\alpha) \\ 0 & 1 & 0 \\ -\sin(\alpha) & 0 & \cos(\alpha) \end{pmatrix} \text{ and} \quad (37)$$

$$\mathbf{R}(\omega, t) = \begin{pmatrix} e^{-(t/T_2)} \cos(\omega t) & e^{-(t/T_2)} \sin(\omega t) & 0 \\ -e^{-(t/T_2)} \sin(\omega t) & e^{-(t/T_2)} \cos(\omega t) & 0 \\ 0 & 0 & e^{-(t/T_1)} \end{pmatrix}. \quad (38)$$

Furthermore, it is convenient to introduce the column vectors

$$\mathbf{\Lambda}(t) = M_0 \begin{pmatrix} 0 \\ 0 \\ 1 - e^{-(t/T_1)} \end{pmatrix}, \quad \mathbf{Q} = \begin{pmatrix} 1 \\ i \\ 0 \end{pmatrix}. \quad (39)$$

The steady state is characterized by the condition  $\mathbf{S}_{n+1} = \mathbf{S}_n$ . The time evolution of the SSFP signal for a fixed offset frequency  $\omega$  can thus be yielded as:

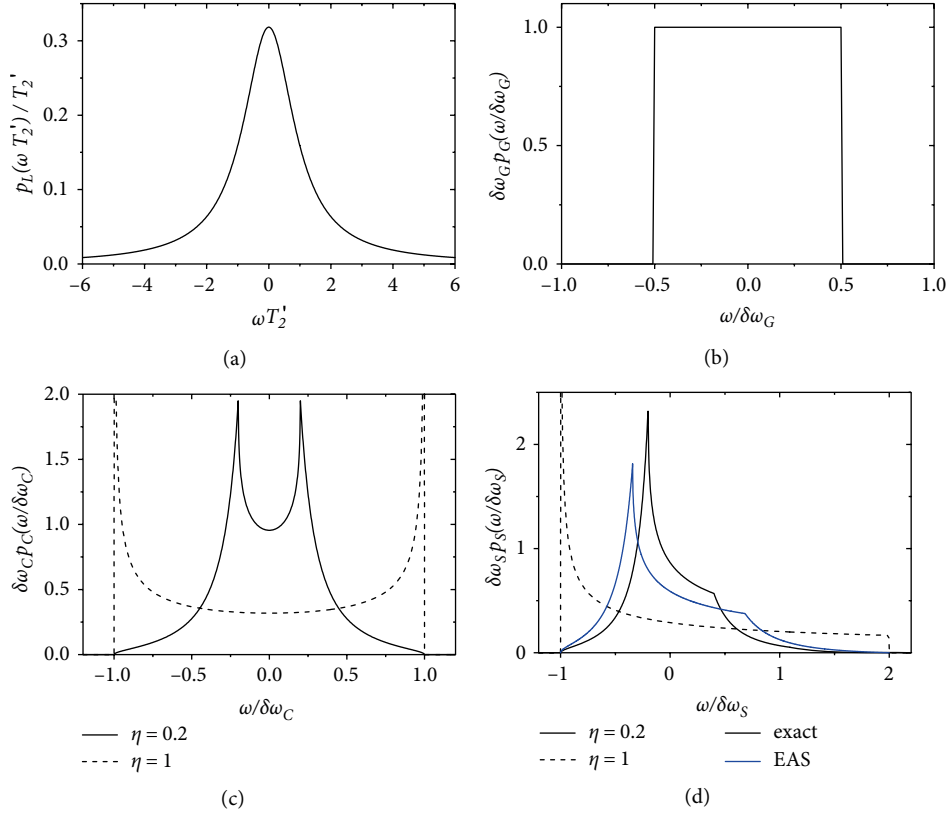


FIGURE 3: Lineshapes for a Lorentzian frequency distribution (a) according to Equation (3), for dephasing in a constant gradient (b) according to Equation (11), for dephasing around a cylinder (c) according to Equation (12), and for dephasing around a sphere (d) according to Equations (13) and (15).

$$\mathbf{S}(\omega, t) = \mathbf{R}(\omega, t) \cdot [\mathbf{I} - \mathbf{P} \cdot \mathbf{R}(\omega, T_R)]^{-1} \cdot \mathbf{P} \cdot \mathbf{\Lambda}(T_R) + \mathbf{\Lambda}(t), \quad (40)$$

where  $\mathbf{I}$  denotes the identity matrix. The inclusion of alternating phases is conceptually analogous. Finally, the complex-valued SSFP signal  $S(t) = S_x(t) + iS_y(t)$  is obtained by a weighted integration of  $\mathbf{S}(\omega, t)$  according to the lineshape  $p(\omega)$ :

$$S(t) = \int_{-\infty}^{+\infty} d\omega p(\omega) \mathbf{Q}^T \cdot [\mathbf{R}(\omega, t) \cdot [\mathbf{I} - \mathbf{P} \cdot \mathbf{R}(\omega, T_R)]^{-1} \cdot \mathbf{P} \cdot \mathbf{\Lambda}(T_R) + \mathbf{\Lambda}(t)]. \quad (41)$$

This integral is numerically calculated for the constant gradient lineshape, the alveolar surface model as well the Lorentzian lineshape and agrees with the theoretically derived signals in all models. Moreover, Equation (24) is used to recalculate the SSFP signal in all models obtaining the same results. This demonstrates the validity of the theoretical approach.

**3.6. Experimental Verification.** Measurements were performed on a 7 Tesla Bruker Biospec 70/30 (Ettlingen, Germany). A 5mm water-filled MR tube axially aligned at the center line of the magnet with the relaxation times  $T_1 = 3.2$  s and  $T_2 = 0.4$  s was measured with a spectroscopic bSSFP pulse sequence [48] with alternating as well as constant phases. After carefully shimming the sample leading to a linewidth

of approximately 4 Hz, a constant gradient was superimposed leading to  $\delta\omega_G = 177$  Hz (value obtained from the bSSFP frequency profile) according to Equation (6). The SSFP sequence parameters were: flip angle  $\alpha = 25^\circ$ , repetition time  $T_R = 25$  ms. In Figure 7, the measured signal is compared with the exact expression of the SSFP signal for a constant gradient according to Equation (32) as well as the SSFP signal expected for a Lorentzian lineshape (see Equation (26)). The theoretically predicted SSFP signal describes the data very well (note that no fit was used), whereas the Lorentzian lineshape model exhibits large deviations from the measured data.

**3.7. Relaxation Time Estimation and Adjustment of Sequence Parameters.** To estimate the impact of the presented results on the relaxation time determination, a simple numerical model is analyzed: we assume tissue that produces a boxcar lineshape with a width of  $\delta\omega_G$  (see Equation (11)) and calculate the SSFP signal according to Equation (32). Then the SSFP signal obtained for a Lorentzian lineshape is fitted to the calculated SSFP signal and the obtained  $T_2'$  relaxation times are compared with the ground truth obtained from Equation (C.4). Thus, the simulation assesses the bias of  $T_2'$  when fitting with a Lorentzian lineshape even though the tissue causes a more complicated lineshape (like the boxcar function). The results are shown in Figure 8(a). For small gradient strengths  $\delta\omega_G$ , the relaxation time  $T_2'$  is highly overestimated, especially for short repetition times  $T_R$ . Only for gradient strength  $\delta\omega_G \lesssim 1/T_R$

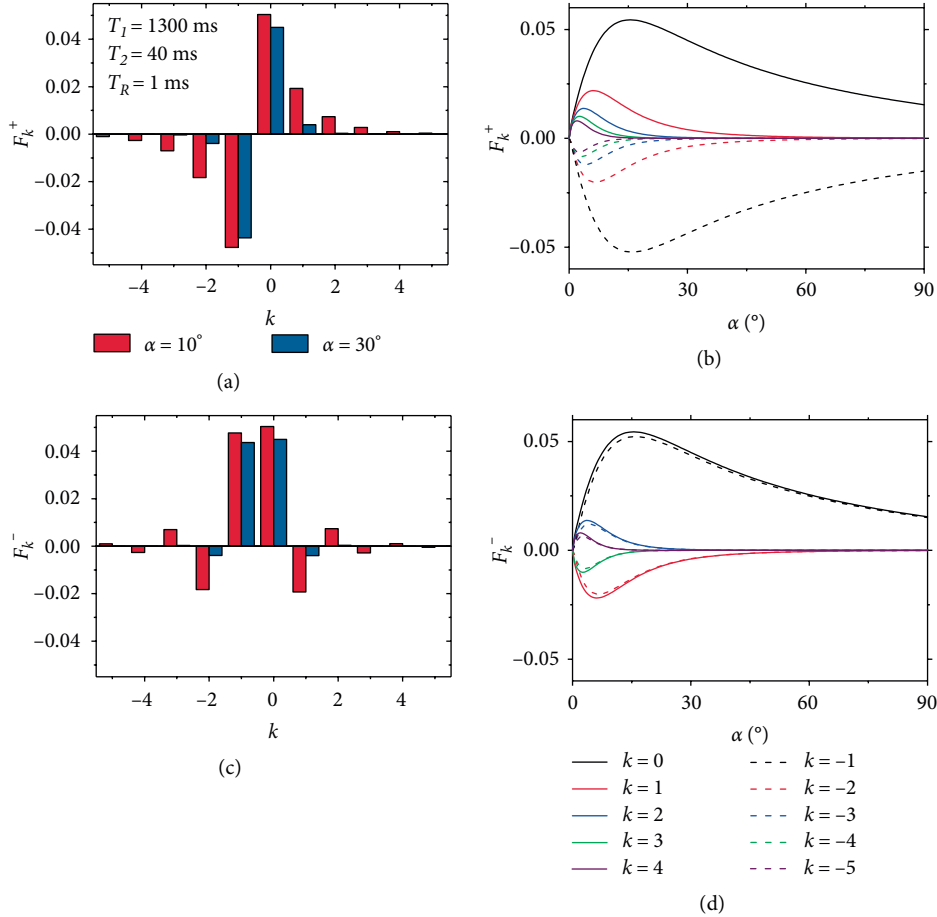


FIGURE 4: Fourier coefficients  $F_k^+$  (a), (b), and  $F_k^-$  (c), (d) obtained from Equation (21) for different flip angles  $\alpha$  for typical parameters of lung tissue ( $T_1 = 1300$  ms,  $T_2 = 40$  ms and  $T_R = 1$  ms).

the fitted relaxation times are similar to the ground truth and, in this regime, the error is in the order of 10%. These results suggest that the exact form of the lineshape has an important influence on the SSFP signal and should in general not be described by a simple Lorentzian lineshape. Furthermore, we assess the accuracy of the  $T_2'$  estimation in the lung. Therefore, the SSFP signal in the alveolar surface model is calculated according to Equation (34) for typical lung parameters of  $T_1 = 1.3$  s and  $T_2 = 0.04$  s. The flip angle was chosen as  $\alpha = 14^\circ$  in accordance with the maximum of the initial signal  $S_{AS,0}^-$  (similar to Figure 6). The calculated SSFP signal was fitted with the biexponential Lorentzian SSFP model (according to Equation (26)) yielding an estimation for the relaxation time  $T_2'$ . The estimated relaxation times are compared with the ground truth obtained from Equation (C.7) and presented in Figure 8(b). Similar to the results for the constant gradient SSFP model, a large bias in the order of 25% occurs for the determination of the relaxation time  $T_2'$ . This result also demonstrates the importance of using the correct form of the lineshape rather than its Lorentzian approximation.

In this work, more realistic lineshape models were analyzed to overcome the drawbacks of the Lorentzian lineshape model. The SSFP signal in the constant gradient model *e.g.*

depends on the parameters  $T_1$ ,  $T_2$ , and  $\delta\omega_G$ . In this model, the frequency offset  $\delta\omega_G$  corresponds to the relaxation time  $T_2'$  via Equation (C.4).

To assess the expected precision and accuracy of determining the parameters in this model, the SSFP signal for a constant gradient was calculated according to Equation (32) for the parameters  $T_1 = 3.2$  s,  $T_2 = 0.4$  s, and  $\delta\omega_G = 175$  Hz motivated by the parameters in Figure 7. Assumed sequence parameters were  $T_R = 25$  ms and  $\alpha = 25^\circ$ . Then, Gaussian noise with standard deviation  $\sigma$  was added and the constant gradient model was fitted to the simulated data for 100 different noise realization per chosen noise level. The obtained values for the above parameters are shown in Figure 9 in dependence on the signal to noise ratio  $\text{SNR} = S(0)/\sigma$ . For the chosen ground truth, the parameters  $T_1$  and  $T_2$  show a high spread for  $\text{SNR}$  lower than 100, whereas the determination of  $\delta\omega_G$  is very precise and accurate for all shown  $\text{SNR}$  values. For  $\text{SNR} > 150$ , all three parameters can accurately and precisely be determined.

#### 4. Discussion and Conclusion

In this work, the signal formation in local magnetic field inhomogeneities is recapitulated. Important local magnetic field



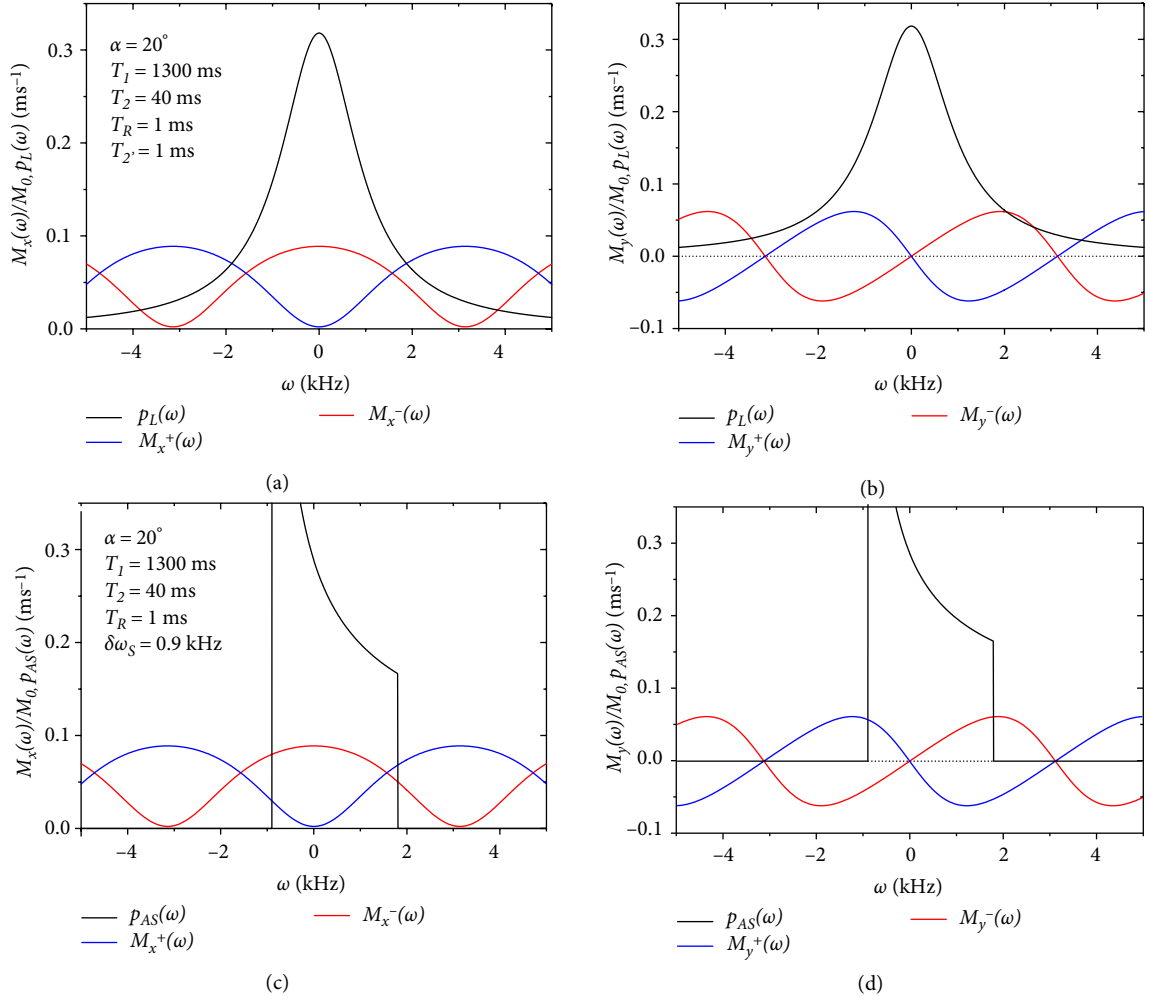


FIGURE 5: Transverse components  $M_x(\omega)$  in (a) and (c) as well as  $M_y(\omega)$  in (b) and (d) for alternating phase (blue lines) and constant phase (red lines) according to Equation (16). The Lorentzian lineshape  $p_L(\omega)$  according to Equation (3) is shown in the black lines in (a) and (b) and the lineshape  $p_{AS}(\omega)$  for dephasing on the alveolar surface according to Equation (14) is shown in the black lines in (c) and (d).

inhomogeneities for magnetic resonance imaging are the constant gradient and dipole fields caused by cylindrical or spherical objects. For these cases, the free induction decay, the corresponding lineshape as well as the SSFP signal are analyzed.

The lineshape for a constant gradient and for cylindrical objects are symmetric. Consequently, the free induction decay as well as the SSFP signal become purely real meaning that only the transverse component  $M_x(t)$  is present while  $M_y(t)$  vanishes. In comparison, the lineshape around spherical objects shows a prominent asymmetry that arises from the angular dependency  $\propto 3 \cos^2(\theta) - 1$ . Therefore, both transverse components of the free induction decay and SSFP signal need to be considered and the signal is complex-valued. It is convenient to introduce a complex  $T_2'$ -time as given in Equation (C.2): its real part describes the decay of the signal amplitude, and the imaginary part the phase oscillation, respectively.

Lung tissue consists of very densely packed air-filled alveoli [49, 50]. The susceptibility difference to the surrounding tissue causes strong susceptibility effects that can be described in the alveolar surface model [18]. In this model, spin-bearing particles are assumed to be located on the surface of a spherical alveolus. In general, contributions to the local Larmor frequency from other alveoli need to be considered. However, numerical simulations show that these contributions are mostly averaged out due to the angular dependency of the Larmor frequency. Details are provided in [18]. In this work, the alveolar surface model was used to predict the SSFP signal in lung tissue. Due to the prominent asymmetry of the lineshape (see Figure 3), the SSFP signal exhibits both transversal components.

The initial SSFP signal  $S_0^+$  is shown in Figure 6 for the Lorentzian lineshape as well as in the alveolar surface model. Since the initial signal is closely related to the signal to noise ratio, flip angle  $\alpha$  and repetition time  $T_R$  should be chosen to

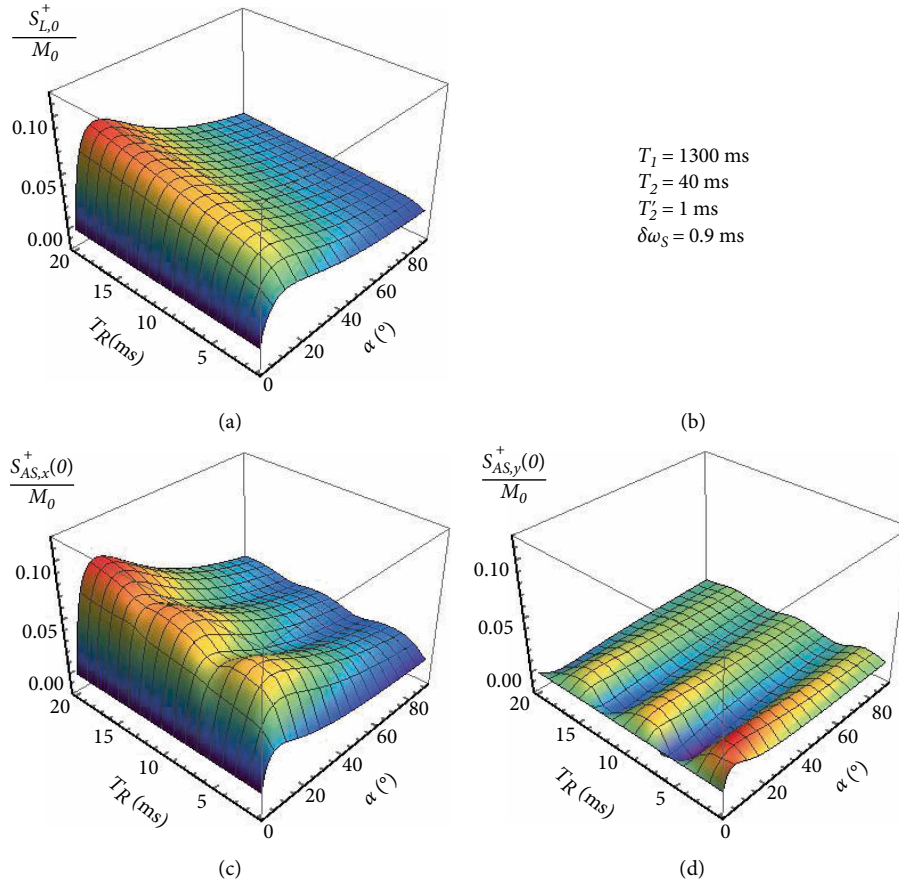


FIGURE 6: Comparison between Lorentzian lineshape and alveolar surface model. The initial signal is shown in dependence on repetition time  $T_R$  and flip angle  $\alpha$  for a Lorentzian lineshape (a) obtained from Equation (29) with the parameters given in (b). (c, d) The  $x$ - and  $y$ -components for the alveolar surface are obtained from Equation (35) for the same parameters.

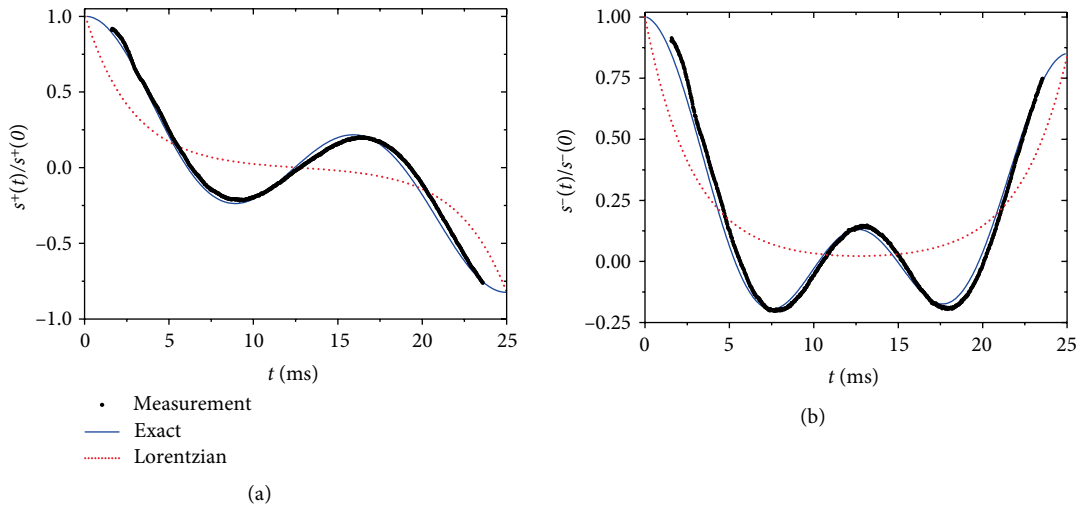


FIGURE 7: Measured SSFP signal (black dots) in a constant gradient field compared with the theoretical predictions assuming a boxcar lineshape (see Equation (32) and blue solid line) and a Lorentzian lineshape (see Equation (26) and red dotted line). This figure shows the need to predict the SSFP signal using the exact form of the lineshape rather than its Lorentzian approximation.

maximize the initial signal. Thus, the alveolar surface model allows optimizing the sequence parameters. A quantitative evaluation of Figure 6 yields a difference of the optimal value

of the flip angle  $\alpha$  in alveolar surface and Lorentzian lineshape model of a few degrees, depending on the chosen repetition time  $T_R$ .

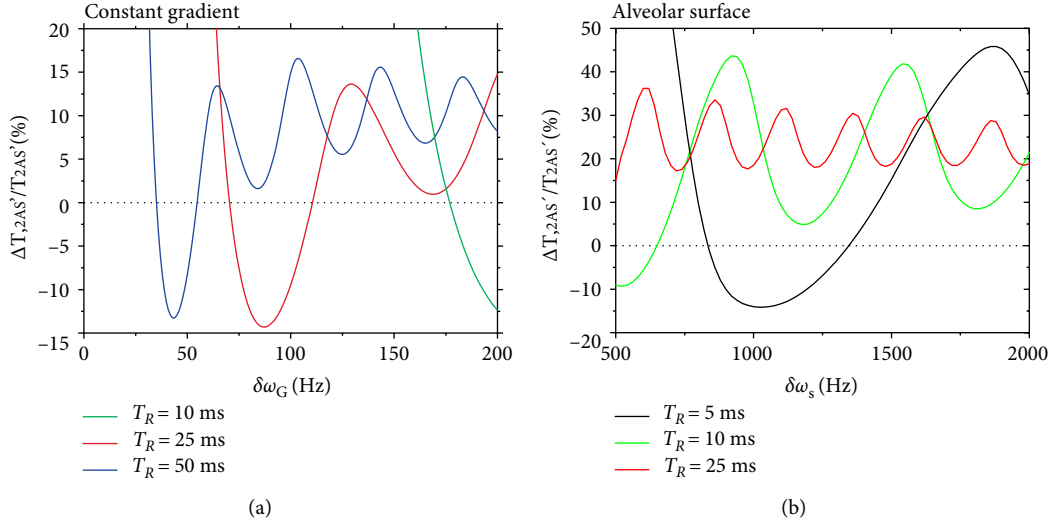


FIGURE 8: Bias of the  $T_2'$  estimation for a tissue with (a) boxcar lineshape  $p_G(\omega)$ , and (b) an alveolar surface lineshape  $p_{AS}(\omega)$ . Both SSFP signals are fitted by the simplified Lorentzian lineshape model. Assumed parameters were  $\alpha = 25^\circ$ ,  $T_1 = 3.2$  s,  $T_2 = 0.4$  s for the boxcar model and  $\alpha = 14^\circ$ ,  $T_1 = 1.3$  s,  $T_2 = 0.04$  s for the alveolar surface model, respectively. The relaxation time  $T_{2G}'$  of the boxcar lineshape depends on the width  $\delta\omega_G$  as given in Equation (C.4) and the relaxation time  $T_{2AS}'$  for the alveolar surface model is determined by the frequency offset  $\delta\omega_{AS}$  (see Equation (C.7)). The figure is shown for constant phases of the rf pulses.

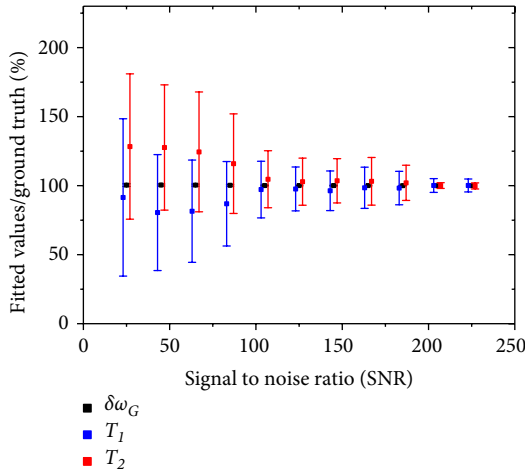


FIGURE 9: Expected accuracy and precision of  $T_1$ ,  $T_2$  and  $\delta\omega_G$  (corresponding to  $T_2'$  according to Equation (C.4)) for the constant gradient model and various signal to noise ratios. The expected ground truth was set to (following the values in Figure 6)  $T_1 = 3.2$  s,  $T_2 = 0.4$  s and  $\delta\omega_G = 175$  Hz. Sequence parameters are  $T_R = 25$  ms and  $\alpha = 25^\circ$ . For SNR > 150, a precise and accurate determination of all three parameters is possible. The figure is shown for constant phases of the rf pulses.

The analytical description of the SSFP signal derived in this work is validated with experimental measurements for a constant field gradient, see Section 3.6. The obtained measurements agree very well with the analytical description for the constant gradient, see Figure 7. Moreover, it becomes obvious that a quantitative description of the SSFP signal needs to account for the exact form of the lineshape, as the Lorentzian lineshape theory predicts a qualitatively different signal.

As a consequence of these findings, the determination of the relaxation time  $T_2'$  has to be performed with the correct lineshape model as shown in Figure 8(a). In this figure, the relative error of  $T_2'$  is shown by fitting the SSFP signal of a constant field gradient with a Lorentzian lineshape. Obviously, large errors can occur, especially for small field gradients and small repetition times  $T_R$ , which are usually preferred to circumvent banding artifacts. This region, where the relaxation time  $T_2'$  is overestimated, can be qualitatively understood since the SSFP signal for a weak constant gradient increases for short times, which cannot be described by the SSFP signal for the Lorentzian lineshape. Similar results are shown in Figure 8(b) where the SSFP signal in the alveolar surface model is fitted by the Lorentzian lineshape model. Hereby, a bias of the determined relaxation time  $T_2'$  in the order of 25% occurs.

In Figure 8, the  $T_2'$  relaxation time was fitted, keeping  $T_1$  and  $T_2$  fixed. In principle, it is possible to simultaneously fit all three parameters. However, the SSFP signal for the Lorentzian lineshape yields a biexponential signal model (see Equation (26)) which is difficult to handle and typically converges to local minima. This is a further drawback of the Lorentzian lineshape approximation. Thus, the correct lineshape model has to be considered.

This also indicates that SSFP sequences in qBOLD imaging might be interesting as they are very sensitive towards changes in the lineshape. The lineshape in blood vessel networks, on the other hand, is sensitive towards changes of physiological parameters like the blood volume fractions or the oxygenation level.

In Figure 9, expected accuracy and precision for determining  $T_1$ ,  $T_2$ , and  $T_2'$  with the constant gradient model are shown in dependence on the signal to noise ratio. Even though the results highly depend on the chosen ground truth values, the relaxation times seems to be robustly measurable for

SNR  $\geq 150$ . A further evaluation for different ground truth values, however, is numerically costly.

In this work, the SSFP signal is analyzed for nonhomogeneous tissue. For a purely monoexponential free induction decay, the lineshape is Lorentzian and the SSFP signal can be calculated by utilizing the Fourier coefficients. However, even for nonexponential signal decay that may occur due to two-dimensional or three-dimensional dipole fields in muscle or lung tissue, the SSFP signal can analytically expressed in terms of the Fourier coefficients. The relaxation times can also be determined for nonLorentzian lineshapes by utilizing the correct lineshape model.

## Appendix

### A. Time Evolution of the Magnetization

For analysis of the local magnetization, it is advantageous to combine the  $x$ - and  $y$ -components of the local transverse magnetization density inside an imaging voxel to a complex-valued quantity

$$m(\mathbf{r}, t) = m_x(\mathbf{r}, t) + im_y(\mathbf{r}, t). \quad (\text{A.1})$$

In general, the time evolution of this local transverse magnetization density is then governed by the Bloch equation

$$\frac{\partial}{\partial t} m(\mathbf{r}, t) = -i\omega(\mathbf{r})m(\mathbf{r}, t), \quad (\text{A.2})$$

where  $\omega(\mathbf{r})$  is the time-independent local Larmor frequency. After an excitation pulse with flip angle  $\alpha$ , the initial transverse magnetization density is assumed to be spatially constant  $m(\mathbf{r}, 0) = m_0 \sin(\alpha)$  and the time evolution of the local transverse magnetization density is given by

$$m(\mathbf{r}, t) = m(\mathbf{r}, 0)e^{-i\omega(\mathbf{r})t}. \quad (\text{A.3})$$

The total magnetization can be obtained by an integration of the local magnetization density over the voxel with volume  $V$ :

$$M(t) = \int_V d^3\mathbf{r} m(\mathbf{r}, t) \quad (\text{A.4})$$

with the total initial magnetization

$$M_0 = m_0 V, \quad (\text{A.5})$$

which will produce the transverse magnetization  $M(0) = M_0 \sin(\alpha)$  after the application of an  $\alpha$ -pulse. Due to the exclusion of the  $T_2$ -relaxation in the definition of the magnetization  $M(t)$ , see Equation (1), the local magnetization  $m(\mathbf{r}, t)$  excludes the intrinsic  $T_2$ -relaxation processes as well. Since the total magnetization is in general complex-valued  $M(t) = M_x(t) + iM_y(t)$ , it is advantageous to consider the lineshape

$$p(\omega) = \frac{1}{2\pi} \int_{-\infty}^{+\infty} \frac{M(t)}{M(0)} e^{+i\omega t} dt. \quad (\text{A.6})$$

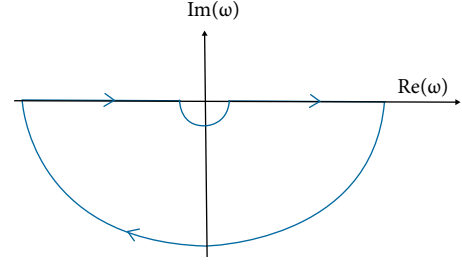


FIGURE 10: Integration pathway according to the right hand side of Equation (C.2).

To obtain a purely real lineshape, it is necessary to continue the magnetization for negative times in the form of

$$M(-t) = M^*(+t). \quad (\text{A.7})$$

Thus, the lineshape can be written as

$$p(\omega) = \frac{1}{\pi} \int_0^{\infty} \text{Re} \left( \frac{M(t)}{M(0)} e^{i\omega t} \right) dt, \quad (\text{A.8})$$

which requires only the knowledge of the magnetization for positive times. Introducing the expression for the total magnetization in Equation (A.4) with the local magnetization in Equation (A.3) into the general definition of the lineshape defined in Equation (A.6) results in

$$p(\omega) = \frac{1}{V} \int_V d^3\mathbf{r} \delta(\omega - \omega(\mathbf{r})), \quad (\text{A.9})$$

where the Fourier representation of Diracs delta distribution was used (note that a sign error occurred in Equation (7) in [18]). Obviously, the lineshape fulfills the properties of a probability distribution:

$$\int_{-\infty}^{+\infty} d\omega p(\omega) = 1. \quad (\text{A.10})$$

The magnetization can be expressed as the inverse Fourier transform of the lineshape according to Equation (A.6):

$$\frac{M(t)}{M(0)} = \int_{-\infty}^{+\infty} p(\omega) e^{-i\omega t} d\omega. \quad (\text{A.11})$$

### B. FLASH Signal Decay

The magnetization  $M_G(t)$  that can be measured *e.g.*, with a FLASH sequence for a constant gradient reads:

$$\frac{M_G(t)}{M_G(0)} = \text{sinc} \left( \frac{\delta\omega_G t}{2} \right). \quad (\text{B.1})$$

The magnetization around a two-dimensional dipole field that occurs *e.g.* around vessels was obtained in [8] or Equations (31) and (32) in [51]:

$$\frac{M_C(t)}{M_C(0)} = \frac{h_c(\eta\delta\omega_c t) - \eta h_c(\delta\omega_c t)}{1 - \eta} \quad (\text{B.2})$$

with the generalized hypergeometric function

$$h_C(x) = {}_1F_2\left(-\frac{1}{2}; \frac{1}{2}, 1; -\left[\frac{x}{2}\right]^2\right). \quad (\text{B.3})$$

An alternative expression for the magnetization decay is given in Equations (39) and (40) in [11].

The magnetization around a three-dimensional dipole field (as present around magnetized particles or alveoli in the lung) reads:

$$\frac{M_S(t)}{M_S(0)} = \frac{h_S(\eta\delta\omega_S t) - \eta h_S(\delta\omega_S t)}{1 - \eta} \quad (\text{B.4})$$

with the function

$$h_S(x) = {}_1F_1\left(\frac{1}{2}; \frac{3}{2}; 3ix\right) + x \int_0^1 dz [3z^2 - 1] \cdot [\text{Si}(x[3z^2 - 1]) - i\text{Ci}(x|3z^2 - 1|)], \quad (\text{B.5})$$

where  ${}_1F_1$  denotes the generalized hypergeometric function and Si and Ci are sine and cosine integral. An alternative expression for the magnetization decay is given in Equation (34) in [52].

In the limit of restricting water molecules to the surface of the alveoli, the time evolution of the magnetization is given by:

$$\frac{M_{AS}(t)}{M_{AS}(0)} = \frac{1+i}{2} \sqrt{\frac{\pi}{6}} \frac{e^{i\delta\omega_S t}}{\sqrt{\delta\omega_S t}} \text{erfi}\left([1-i] \sqrt{3\delta\omega_S \frac{t}{2}}\right), \quad (\text{B.6})$$

where  $\text{erfi}(z) = -i\text{erf}(iz)$  denotes the imaginary error function. This expression also follows from the magnetization decay caused by a spherical object given in Equation (B.4) in the limit  $\eta \rightarrow 1$ , when dephasing occurs on the surface of the sphere:  $M_{AS}(t) = \lim_{\eta \rightarrow 1} M_S(t)$ .

In the extended alveolar surface model, the magnetization reads:

$$\frac{M_{EAS}(t)}{M_{EAS}(0)} = \frac{h_{EAS}(\eta^{2/3}\delta\omega_S t) - \eta h_{EAS}(\delta\omega_S t)}{1 - \eta} \quad (\text{B.7})$$

with  $h_{EAS}(x)$  given in Equation (C.10) in [31]:

$$h_{EAS}(x) = e^{-2ix} + e^{ix}[1+i] \sqrt{\frac{\pi x}{6}} \text{erf}\left([1+i] \sqrt{\frac{3x}{2}}\right) + \sqrt{2\pi}[1-i]x^{3/2} \cdot \int_0^1 dy [3y^2 - 1]^{3/2} \text{erf}\left([1+i] \sqrt{x \frac{3y^2 - 1}{2}}\right). \quad (\text{B.8})$$

## C. Monoexponential Approximation

In general, the magnetization  $M(t)$  exhibits decaying and oscillating parts and thus, is nonmonoexponential. However, for some applications it might be advantageous to define a monoexponential approximation time  $T'_2$ . The relaxation time  $T'_2$  can be obtained in terms of a mean relaxation time approximation [13]:

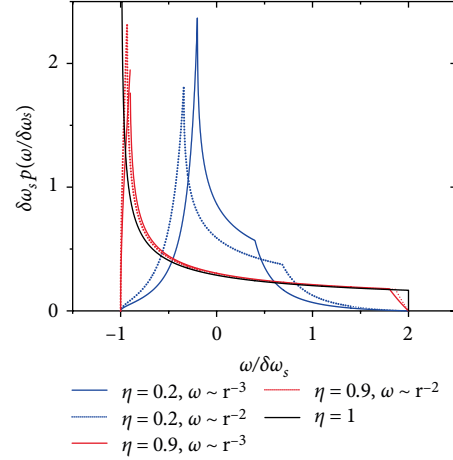


FIGURE 11: Comparison of lineshapes in the static dephasing for the exact dipole field  $\omega_S(r, \theta) = \delta\omega_S R_S^3 [3\cos^2(\theta) - 1]/r^3$  according to Equation (13), the alveolar surface model  $\omega_{AS}(\theta) = \delta\omega_S [3\cos^2(\theta) - 1]$  given in Equation (14), and the extended alveolar surface model  $\omega_{EAS}(r, \theta) = \delta\omega_S R_S^2 [3\cos^2(\theta) - 1]/r^2$  given in Equation (15). The lineshapes for the exact dipole field are obtained from Equation (13) for  $\eta = 0.2$  shown as blue solid line and for  $\eta = 0.9$  as red solid line. The lineshapes in the extended alveolar surface model are obtained from Equation (15) for  $\eta = 0.2$  (blue dotted line) and for  $\eta = 0.9$  (red dotted line). The black solid line shows the lineshape in the limit  $\eta = 1$  obtained from Equation (14) that corresponds to the alveolar surface model.

$$T'_2 = \int_0^\infty dt \frac{M(t)}{M(0)}. \quad (\text{C.1})$$

The range correctly described by the mean time approximation depends on the actual form of the magnetization  $M(t)$  as analyzed in [53]. Since the magnetization can be expressed in terms of the lineshape according to Equation (A.11), the relaxation time can also be expressed in terms of the lineshape:

$$T'_2 = \pi p(0) - i \int_{-\infty}^\infty d\omega \frac{p(\omega)}{\omega} = -i \oint d\omega \frac{p(\omega)}{\omega}, \quad (\text{C.2})$$

where the pathway of integration is visualized in Figure 10. In the static-dephasing regime, the lineshape can be expressed directly in terms of the local Larmor frequency according to Equation (A.9) which allows to obtain an expression of the transverse relaxation time in the form of

$$T'_2 = \frac{1}{V} \int_V d^3 \mathbf{r} \left[ \pi \delta(\omega(\mathbf{r})) + \frac{i}{\omega(\mathbf{r})} \right]. \quad (\text{C.3})$$

The real part of the relaxation time  $T'_2$  describes the signal loss, whereas the imaginary part describes the oscillatory behavior of the phase.

Applying Eq. (C.1) or Eq. (C.2), the transverse relaxation times for the different geometries presented follows as

$$T'_{2G} = \frac{\pi}{\delta\omega_G}, \quad (\text{C.4})$$

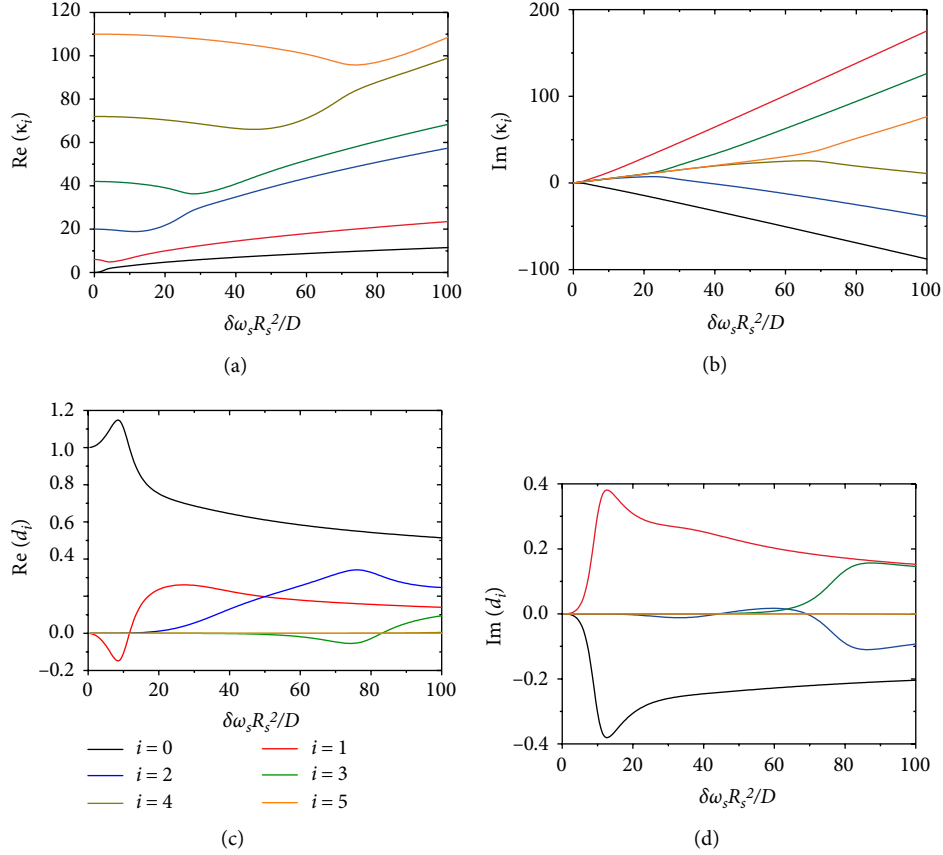


FIGURE 12: Eigenvalues  $\kappa_i$  and expansion coefficients  $d_i$  in dependence on the parameter  $\delta\omega_s R_s^2/D$  according to Equation (E.3) for real part (a) and imaginary part (b) of the eigenvalues and according to Equation (E.4) for real part (c) and imaginary part (d) of the expansion coefficients.

$$T'_{2C} = \frac{1 + \eta}{2\eta\delta\omega_s}, \quad (\text{C.5})$$

$$T'_{2S} = \frac{\pi + i \ln(2 + \sqrt{3})}{\delta\omega_s} \frac{1}{4\sqrt{3}} \frac{1 + \eta}{\eta}, \quad (\text{C.6})$$

$$T'_{2AS} = \frac{\pi + i \ln(2 + \sqrt{3})}{\delta\omega_s} \frac{1}{2\sqrt{3}}, \quad (\text{C.7})$$

$$T'_{2EAS} = \frac{\pi + i \ln(2 + \sqrt{3})}{\delta\omega_s} \frac{\sqrt{3}}{10} \frac{\eta^{-2/3} - \eta}{1 - \eta}. \quad (\text{C.8})$$

The transverse relaxation time for a cylinder  $T'_{2C}$  agrees with Equation (19) in [34]. Obviously, the relaxation times for a spherical objects  $T'_{2S}$  as well as in the extended alveolar surface model  $T'_{2EAS}$  converge towards the alveolar surface relaxation time  $T'_{2AS}$  within the limit of large air volume fractions  $\eta \rightarrow 1$ .

## D. Extended Alveolar Surface Model

Within the static dephasing limit, where diffusion is neglected, the lineshape in the extended alveolar surface model is given in Equation (15) where the function  $f(\omega/\delta\omega_s)$  can be found as:

$$f\left(\frac{\omega}{\delta\omega_s}\right) = \begin{cases} \sqrt{-\frac{\delta\omega_s}{\omega}} \left[ \frac{\pi}{2} - \arcsin\left(\sqrt{-\frac{\omega}{\delta\omega_s}}\right) \right] & \text{for } -1 \leq \frac{\omega}{\delta\omega_s} \leq -\eta^{2/3}, \\ \left[ \frac{1}{\eta} \frac{2}{3} \frac{\omega}{\delta\omega_s} - \frac{1}{\sqrt[3]{\eta}} \right] \sqrt{1 + \eta^{-2/3} \frac{\omega}{\delta\omega_s}} + \sqrt{\frac{\delta\omega_s}{\omega}} \ln\left(\frac{\eta^{-(1/3)} + \sqrt{\eta^{-(2/3)} + (\delta\omega_s/\omega)}}{1 + \sqrt{1 + \delta(\omega_s/\omega)}}\right) & \text{for } -\eta^{2/3} \leq \frac{\omega}{\delta\omega_s} \leq 2\eta^{2/3}, \\ \sqrt{\frac{\delta\omega_s}{\omega}} \left[ \frac{\sqrt{6}}{3} + \ln\left(\sqrt{\frac{\delta\omega_s}{\omega}} \frac{\sqrt{2 + \sqrt{3}}}{1 + \sqrt{1 + (\delta\omega_s/\omega)}}}\right) \right] & \text{for } 2\eta^{2/3} \leq \frac{\omega}{\delta\omega_s} \leq 2. \end{cases} \quad (\text{D.1})$$

A comparison of the lineshapes for the exact three-dimensional dipole field and the extended alveolar surface model is shown in Figure 11.

## E. Diffusion Effects

If diffusion effects are included, an additional diffusion term has to be added to the original Bloch equation (A.2) which leads to the Bloch–Torrey equation [54]

$$\frac{\partial}{\partial t} m(\mathbf{r}, t) = [D\Delta - i\omega(\mathbf{r})]m(\mathbf{r}, t). \quad (\text{E.1})$$

Analytical solutions for this partial differential equation can be given for diffusion in a constant gradient as given in Equation (6) in terms of Airy-functions [32, 33], for diffusion around a two-dimensional dipole field [55, 56] as given in Equation (7) in terms of Bessel-functions [57] and Mathieu-functions [58]. For dephasing on the alveolar surface as given in Equation (9), the signal evolution can be expressed in terms of spheroidal wave functions [18]. The corresponding lineshape for diffusion on the alveolar surface takes the asymmetric form of

$$p_A(\omega) = \frac{1}{\pi} \frac{R_S^2}{D} \sum_{l=0}^{\infty} \frac{\text{Re}(d_l \kappa_l^*) - \omega(R_S^2/D) \text{Im}(d_l)}{|\kappa_l|^2 - 2\omega(R_S^2/D) \text{Im}(\kappa_l) + \left[\omega \frac{R_S^2}{D}\right]^2} \quad (\text{E.2})$$

with eigenvalues  $\kappa_l$  and expansion coefficients  $d_l$ :

$$\kappa_l = 2i\delta\omega_s \frac{R_S^2}{D} + \lambda_{2l,0} \left( \sqrt{3i\delta\omega_s \frac{R_S^2}{D}} \right), \quad (\text{E.3})$$

$$d_l = [4l + 1] \left[ PS_{2l,0} \left( \sqrt{i\delta\omega_s \frac{R_S^2}{D}}, 0 \right) S_{2l,0}^{(1)} \left( \sqrt{i\delta\omega_s \frac{R_S^2}{D}}, 1 \right) \right]^2, \quad (\text{E.4})$$

where  $\lambda_{2l,0}$  are the spheroidal eigenvalues and  $PS_{2l,0}$  as well as  $S_{2l,0}^{(1)}$  are the spheroidal eigenfunctions [18, 59]. Eigenvalues and expansion coefficients are complex quantities and depend on the parameter  $\delta\omega_s R_S^2/D$  only, as visualized in Figure 12. A similar eigenfunction expansion is possible for the Bloch-Torrey equation around vessels [5, 55]. Further approximative methods for the analysis of diffusion effects in magnetic field inhomogeneities are presented in [60–62]. In the static dephasing limit, the lineshape converges to the alveolar surface lineshape  $p_{AS}(\omega)$  given in Equation (14):

$$p_{AS}(\omega) = \lim_{\delta\omega_s(R_S^2/D) \rightarrow \infty} p_A(\omega). \quad (\text{E.5})$$

One important issue to be mentioned is the range of possible resonance frequencies for dephasing with and without diffusion. In the static dephasing regime ( $D = 0$ ), the Larmor frequency takes minimal and maximal values which restricts the lineshape to a limited frequency interval, i.e. for dephasing in a constant gradient (see Equation (11) and Figure 3(c)) the lineshape ranges from  $-\delta\omega_G/2 \leq \omega \leq +\delta\omega_G/2$ . For dephasing around a two-dimensional dipole field (see Equation (12) and Figure 3(b)), the lineshape ranges from  $-\delta\omega_C \leq \omega \leq +\delta\omega_C$  and for dephasing around a three-dimensional dipole field (see Equation (13) and Figure 3(d)), the lineshape ranges from  $-\delta\omega_s \leq \omega \leq +2\delta\omega_s$ . If diffusion effects appear, the lineshape is not limited to a finite frequency interval and all possible resonance frequencies must be taken into account similar to the Lorentzian lineshape. The relevant magnetization decay is given by

$$\frac{M_A(t)}{M_A(0)} = \sum_{l=0}^{\infty} d_l e^{-\kappa_l(Dt/R_S^2)}. \quad (\text{E.6})$$

Since the imaginary parts of the eigenvalues  $\kappa_l$  and of the expansion coefficients  $d_l$  never vanish (see Figures E.12(b) and E.12(d)), the lineshape according to Equation (E.2) is not a simple linear combination of Lorentzian lineshapes.

The transverse relaxation time in the alveolar surface model for nonvanishing diffusion effects  $T'_{2A}$  can easily be obtained from the mean relaxation time approximation by introducing Equation (E.6) into Equation (C.1) or from the lineshape given in Equation (E.2) with Equation (C.2):

$$T'_{2A} = \frac{R_S^2}{D} \sum_{l=0}^{\infty} \frac{d_l}{\kappa_l}. \quad (\text{E.7})$$

## Data Availability

The data used to support the findings of this study are available from the corresponding author upon request.

## Conflicts of Interest

The authors declare that they have no conflicts of interest.

## Authors' Contributions

C. H. Ziener and M. Uhrig are contributed equally.

## Acknowledgments

This work was supported by grants from the Deutsche Forschungsgemeinschaft (Contract Grant number: DFG ZI 1295/2-1 and DFG KU 3555/1-1). T. Kampf and M. Pham were supported by the Heidelberg Pain Consortium (SFB 1158). V. J. F. Sturm was supported by the Deutsche Forschungsgemeinschaft (SFB 1118/2).

## References

- [1] D. Ma, V. Gulani, N. Seiberlich et al., "Magnetic resonance fingerprinting," *Nature*, vol. 495, no. 7440, pp. 187–192, 2013.
- [2] X. He, M. Zhu, and D. A. Yablonskiy, "Validation of oxygen extraction fraction measurement by qBOLD technique," *Magnetic Resonance in Medicine*, vol. 60, no. 4, pp. 882–888, 2008.
- [3] J. D. Dickson, T. W. Ash, G. B. Williams, A. L. Sukstanskii, R. E. Ansorge, and D. A. Yablonskiy, "Quantitative phenomenological model of the BOLD contrast mechanism," *Journal of Magnetic Resonance*, vol. 212, no. 1, pp. 17–25, 2011.
- [4] D. A. Yablonskiy, A. L. Sukstanskii, and X. He, "Blood oxygenation level-dependent (BOLD)-based techniques for the quantification of brain hemodynamic and metabolic properties—theoretical models and experimental approaches," *NMR in Biomedicine*, vol. 26, no. 8, pp. 963–986, 2013.
- [5] L. R. Buschle, F. T. Kurz, T. Kampf, H. -P. Schlemmer, and C. H. Ziener, "Spin dephasing around randomly distributed vessels," *Journal of Magnetic Resonance*, vol. 299, pp. 12–20, 2019.

- [6] C. V. Bowen, R. S. Menon, and J. S. Gati, "High field balanced-SSFP fMRI: a BOLD technique with excellent tissue sensitivity and superior large vessel suppression," *Proceedings of the International Society of Magnetic Resonance in Medicine*, p. 119, 2005.
- [7] S. Köhler, K. -H. Hiller, M. Griswold, W. R. Bauer, A. Haase, and P. M. Jakob, "NMR-microscopy with TrueFISP at 11.75 T," *Journal of Magnetic Resonance*, vol. 161, no. 2, pp. 252–257, 2003.
- [8] D. A. Yablonskiy and E. M. Haacke, "Theory of NMR signal behavior in magnetically inhomogeneous tissues: the static dephasing regime," *Magnetic Resonance in Medicine*, vol. 32, no. 6, pp. 749–763, 1994.
- [9] V. G. Kiselev and S. Posse, "Analytical theory of susceptibility induced NMR signal dephasing in a cerebrovascular network," *Physical Review Letters*, vol. 81, no. 25, pp. 5696–5699, 1998.
- [10] J. Sedlacik, A. Rauscher, and J. R. Reichenbach, "Quantification of modulated blood oxygenation levels in single cerebral veins by investigating their MR signal decay," *Zeitschrift für Medizinische Physik*, vol. 19, no. 1, pp. 48–57, 2009.
- [11] L. R. Buschle, C. H. Ziener, K. Zhang et al., "Vessel radius mapping in an extended model of transverse relaxation," *Magnetic Resonance Materials in Physics, Biology and Medicine*, vol. 31, no. 4, pp. 531–551, 2018.
- [12] F. T. Kurz, L. R. Buschle, A. Hahn et al., "Diffusion effects in myelin sheath free induction decay," *Journal of Magnetic Resonance*, vol. 297, pp. 61–75, 2018.
- [13] W. R. Bauer, W. Nadler, M. Bock et al., "The relationship between the BOLD-induced T2 and T2': a theoretical approach for the vasculature of myocardium," *Magnetic Resonance in Medicine*, vol. 42, no. 6, pp. 1004–1010, 1999.
- [14] W. R. Bauer, W. Nadler, M. Bock et al., "Theory of coherent and incoherent nuclear spin dephasing in the heart," *Physical Review Letters*, vol. 83, no. 20, pp. 4215–4218, 1999.
- [15] W. R. Bauer, W. Nadler, M. Bock et al., "Theory of the BOLD effect in the capillary region: an analytical approach for the determination of T2 in the capillary network of myocardium," *Magnetic Resonance in Medicine*, vol. 41, no. 1, pp. 51–62, 1999.
- [16] A. Kjørstad, D. M. R. Corteville, T. Henzler, G. Schmid-Bindert, F. G. Zöllner, and L. R. Schad, "Non-invasive quantitative pulmonary V/Q imaging using Fourier decomposition MRI at 1.5 T," *Zeitschrift fuer Medizinische Physik*, vol. 25, no. 4, pp. 326–332, 2015.
- [17] A. Kjørstad, M. Regier, J. Fiehler, and J. Sedlacik, "A decade of lung expansion: A review of ventilation-weighted 1H lung MRI," *Zeitschrift fuer Medizinische Physik*, vol. 27, no. 3, pp. 172–179, 2017.
- [18] L. R. Buschle, F. T. Kurz, T. Kampf et al., "Dephasing and diffusion on the alveolar surface," *Physical Review E*, vol. 95, no. 2, p. 022415, 2017.
- [19] F. T. Kurz, T. Kampf, L. R. Buschle et al., "Microstructural analysis of peripheral lung tissue through CPMG inter-echo time R2 dispersion," *PLoS One*, vol. 10, no. 11, p. e0141894, 2015.
- [20] R. Mulkern, S. Haker, H. Mamata et al., "Lung parenchymal signal intensity in MRI: A technical review with educational aspirations regarding reversible versus irreversible transverse relaxation effects in common pulse sequences," *Concepts in Magnetic Resonance Part A*, vol. 43A, no. 2, pp. 29–53, 2014.
- [21] J. Zapp, S. Domsch, S. Weingärtner, and L. R. Schad, "Gaussian signal relaxation around spin echoes: implications for precise reversible transverse relaxation quantification of pulmonary tissue at 1.5 and 3 Tesla," *Magnetic Resonance in Medicine*, vol. 77, no. 5, pp. 1938–1945, 2017.
- [22] F. Carinci, C. Meyer, F. A. Breuer, and P. M. Jakob, "In vivo imaging of the spectral line broadening of the human lung in a single breathhold," *Journal of Magnetic Resonance Imaging*, vol. 44, no. 3, pp. 745–757, 2016.
- [23] J. Pintaske, B. Müller-Bierl, and F. Schick, "Field perturbations by magnetic dipoles as a model for magnetically labelled cells in MRI," *Zeitschrift fuer Medizinische Physik*, vol. 16, no. 4, pp. 252–260, 2006.
- [24] C. H. Ziener, W. R. Bauer, and P. M. Jakob, "Transverse relaxation of cells labeled with magnetic nanoparticles," *Magnetic Resonance in Medicine*, vol. 54, no. 3, pp. 702–706, 2005.
- [25] W. R. Bauer, C. H. Ziener, and P. M. Jakob, "Non-Gaussian spin dephasing," *Physical Review A*, vol. 71, no. 5, p. 053412, 2005.
- [26] C. H. Ziener, T. Kampf, V. Herold, P. M. Jakob, W. R. Bauer, and W. Nadler, "Frequency autocorrelation function of stochastically fluctuating fields caused by specific magnetic field inhomogeneities," *The Journal of Chemical Physics*, vol. 129, no. 1, p. 014507, 2008.
- [27] C. Ganter, "Static susceptibility effects in balanced SSFP sequences," *Magnetic Resonance in Medicine*, vol. 56, no. 3, pp. 687–691, 2006.
- [28] E. M. Haacke, M. R. Thompson, R. W. Brown, and R. Venkatesan, *Magnetic Resonance Imaging: Physical Principles and Sequence Design*, Wiley, New York, 1999.
- [29] F. T. Kurz, T. Kampf, L. R. Buschle et al., "CPMG relaxation rate dispersion in dipole fields around capillaries," *Magnetic Resonance Imaging*, vol. 34, no. 7, pp. 875–888, 2016.
- [30] G. Klug, T. Kampf, C. Ziener et al., "Murine atherosclerotic plaque imaging with the USPIO Ferumoxtran-1010," *Frontiers in Bioscience*, vol. 14, pp. 2546–2552, 2009.
- [31] C. H. Ziener, T. Kampf, F. T. Kurz, H. -P. Schlemmer, and L. R. Buschle, "Pseudo-diffusion effects in lung MRI," *Journal of Magnetic Resonance*, vol. 299, pp. 1–11, 2019.
- [32] S. D. Stoller, W. Happer, and F. J. Dyson, "Transverse spin relaxation in inhomogeneous magnetic fields," *Physical Review A*, vol. 44, no. 11, pp. 7459–7477, 1991.
- [33] M. Herberthson, E. Özarslan, H. Knutsson, and C. F. Westin, "Dynamics of local magnetization in the eigenbasis of the Bloch–Torrey operator," *The Journal of Chemical Physics*, vol. 146, no. 12, p. 124201, 2017.
- [34] C. H. Ziener, W. R. Bauer, and P. M. Jakob, "Frequency distribution and signal formation around a vessel," *Magnetic Resonance Materials in Physics, Biology and Medicine*, vol. 18, no. 4, pp. 225–230, 2005.
- [35] J. Sedlacik, A. Rauscher, and J. R. Reichenbach, "Obtaining blood oxygenation levels from MR signal behavior in the presence of single venous vessels," *Magnetic Resonance in Medicine*, vol. 58, no. 5, pp. 1035–1044, 2007.
- [36] F. T. Kurz, C. H. Ziener, M. Rückl et al., "The influence of spatial patterns of capillary networks on transverse relaxation," *Magnetic Resonance Imaging*, vol. 40, pp. 31–47, 2017.
- [37] L. R. Buschle, T. Kampf, F. T. Kurz et al., "Dependence of the frequency distribution around a vessel on the voxel orientation," *Magnetic Resonance Imaging*, vol. 57, pp. 259–270, 2019.
- [38] Y. C. Cheng, E. M. Haacke, and Y. J. Yu, "An exact form for the magnetic field density of states for a dipole," *Magnetic Resonance Imaging*, vol. 19, no. 7, pp. 1017–1023, 2001.
- [39] C. H. Durney, J. Bertolina, D. C. Ailion et al., "Calculation and interpretation of inhomogeneous line broadening in models of



- lungs and other heterogeneous structures,” *Journal of Magnetic Resonance*, vol. 85, no. 3, pp. 554–570, 1989.
- [40] J. H. Seppenwoolde, M. van Zijtveld, and C. J. Bakker, “Spectral characterization of local magnetic field inhomogeneities,” *Physics in Medicine and Biology*, vol. 50, no. 2, pp. 361–372, 2005.
- [41] K. Scheffler and S. Lehnhardt, “Principles and applications of balanced SSFP techniques,” *European Radiology*, vol. 13, no. 11, pp. 2409–2418, 2003.
- [42] M. Gloor, K. Scheffler, and O. Bieri, “Nonbalanced SSFP-based quantitative magnetization transfer imaging,” *Magnetic Resonance in Medicine*, vol. 64, no. 1, pp. 149–156, 2010.
- [43] M. L. Gyngell, “The steady-state signals in short-repetition-time sequences,” *Journal of Magnetic Resonance (1969)*, vol. 81, no. 3, pp. 474–483, 1989.
- [44] W. Hänicke and H. U. Vogel, “An analytical solution for the SSFP signal in MRI,” *Magnetic Resonance in Medicine*, vol. 49, no. 4, pp. 771–775, 2003.
- [45] D. J. Kim and Z. H. Cho, “Analysis of the higher-order echoes in SSFP,” *Magnetic Resonance in Medicine*, vol. 19, no. 1, pp. 20–30, 1991.
- [46] K. Scheffler and J. Hennig, “Is TrueFISP a Gradient-Echo or a Spin-Echo Sequence?,” *Magnetic Resonance in Medicine*, vol. 49, no. 2, pp. 395–397, 2003.
- [47] B. A. Hargreaves, S. S. Vasanaawala, J. M. Pauly, and D. G. Nishimura, “Characterization and reduction of the transient response in steady-state MR imaging,” *Magnetic Resonance in Medicine*, vol. 46, no. 1, pp. 149–158, 2001.
- [48] W. Dreher, C. Geppert, M. Althaus, and D. Leibfritz, “Fast proton spectroscopic imaging using steady-state free precession methods,” *Magnetic Resonance in Medicine*, vol. 50, no. 3, pp. 453–460, 2003.
- [49] E. Namati, J. Thiesse, J. de Ryk, and G. McLennan, “Alveolar dynamics during respiration: are the pores of Kohn a pathway to recruitment?,” *American Journal of Respiratory Cell and Molecular Biology*, vol. 38, no. 5, pp. 572–578, 2008.
- [50] F. T. Kurz, T. Kampf, S. Heiland, M. Bendszus, H.-P. Schlemmer, and C. H. Ziener, “Theoretical model of the single spin-echo relaxation time for spherical magnetic perturbers,” *Magnetic Resonance in Medicine*, vol. 71, no. 5, pp. 1888–1895, 2014.
- [51] C. H. Ziener, T. Kampf, G. Melkus et al., “Local frequency density of states around field inhomogeneities in magnetic resonance imaging: effects of diffusion,” *Physical Review E*, vol. 76, no. 3, p. 031915, 2007.
- [52] L. R. Buschle, F. T. Kurz, T. Kampf, S. M. F. Triphan, H.-P. Schlemmer, and C. H. Ziener, “Diffusion-mediated dephasing in the dipole field around a single spherical magnetic object,” *Magnetic Resonance Imaging*, vol. 33, no. 9, pp. 1126–1145, 2015.
- [53] W. Nadler and K. Schulten, “Mean relaxation time approximation for dynamical correlation functions in stochastic systems near instabilities,” *Zeitschrift fuer Physik B Condensed Matter*, vol. 72, no. 4, pp. 535–543, 1988.
- [54] H. C. Torrey, “Bloch equations with diffusion terms,” *Physical Review*, vol. 104, no. 3, pp. 563–565, 1956.
- [55] C. H. Ziener, T. Kampf, G. Reents, H. P. Schlemmer, and W. R. Bauer, “Spin dephasing in a magnetic dipole field,” *Physical Review E*, vol. 85, no. 5, p. 051908, 2012.
- [56] C. H. Ziener, F. T. Kurz, and T. Kampf, “Free induction decay caused by a dipole field,” *Physical Review E*, vol. 91, no. 3, p. 032707, 2015.
- [57] C. H. Ziener, F. T. Kurz, L. R. Buschle, and T. Kampf, “Orthogonality, Lommel integrals and cross product zeros of linear combinations of Bessel functions,” *SpringerPlus*, vol. 4, no. 1, p. 390, 2015.
- [58] C. H. Ziener, M. Rückl, T. Kampf, W. R. Bauer, and H. P. Schlemmer, “Mathieu functions for purely imaginary parameters,” *Journal of Computational and Applied Mathematics*, vol. 236, no. 17, pp. 4513–4524, 2012.
- [59] J. Meixner and F. W. Schäfke, *Mathieusche Funktionen und Sphäroidfunktionen*, Springer-Verlag, Berlin Heidelberg, 1954.
- [60] A. L. Sukstanskii and D. A. Yablonskiy, “Gaussian approximation in the theory of MR signal formation in the presence of structure-specific magnetic field inhomogeneities,” *Journal of Magnetic Resonance*, vol. 163, no. 2, pp. 236–247, 2003.
- [61] F. T. Kurz, T. Kampf, L. R. Buschle et al., “Generalized moment analysis of magnetic field correlations for accumulations of spherical and cylindrical magnetic perturbers,” *Frontiers in Physics*, vol. 4, p. 46, 2016.
- [62] C. H. Ziener, T. Kampf, H.-P. Schlemmer, and L. R. Buschle, “Spin dephasing in the gaussian local phase approximation,” *The Journal of Chemical Physics*, vol. 149, no. 24, p. 244201, 2018.

